

Data-processing technique for the Taipan “Be-filter” neutron spectrometer at the Australian Nuclear Science and Technology Organisation

Cite as: *Rev. Sci. Instrum.* **92**, 073304 (2021); doi: [10.1063/5.0054786](https://doi.org/10.1063/5.0054786)

Submitted: 21 April 2021 • Accepted: 25 June 2021 •

Published Online: 9 July 2021



View Online



Export Citation



CrossMark

Gail. N. Iles,^{1,a)}  Kirrily. C. Rule,²  Vanessa. K. Peterson,²  Anton P. J. Stampfl,² 
and Margaret M. Elcombe²

AFFILIATIONS

¹Space Physics Group, School of Science, RMIT University, Melbourne, VIC 3000, Australia

²Australian Nuclear Science and Technology Organisation, Lucas Heights, NSW 2234, Australia

^{a)}Author to whom correspondence should be addressed: gail.iles@rmit.edu.au

ABSTRACT

There are five filter-analyzer neutron spectrometers available worldwide for scientists to use in order to measure the vibrational density of states in various samples. While Taipan, the thermal spectrometer, has been operated as a triple-axis spectrometer at the Australian Centre for Neutron Scattering since 2010, a beryllium filter analyzer spectrometer was added in 2016. Due to the complex nature of the data post-processing, it has thus far been impossible to fully treat experimental data from scientific measurements taken over the last five years. We have successfully created a robust method of treating data from the Taipan filter-analyzer and present the method on three different samples. The data-treatment process includes correction for the non-linear energy variation of a particular monochromator, removal of higher-order wavelength contamination, and estimation of low-energy multiple-scattering. The steps described here can be utilized by all users of the Australian Nuclear Science and Technology Organisation “Be-filter”—past, present, and future.

Published under an exclusive license by AIP Publishing. <https://doi.org/10.1063/5.0054786>

I. INTRODUCTION

The Taipan triple-axis spectrometer was the first inelastic neutron instrument to be commissioned at the Australian Centre for Neutron Scattering (ACNS) (then called the “Bragg Institute”) at the Australian Nuclear Science and Technology Organisation (ANSTO).¹ The original instrument featured a highly ordered pyrolytic graphite (HOPG) monochromator offering an incident energy range of 5–70 meV. In 2015, construction of a low-energy band-pass filter detector was completed, and this new filter-analyzer option entered the user service directly thereafter.² Design of the Taipan filter-analyzer was based on the Filter-Analyzer Neutron Spectrometer (FANS) at the NIST Center for Neutron Research.³ Today, these are the only two filter-analyzer spectrometers in operation with this design in a population of just five Be neutron spectrometers worldwide (Table I).

In each of these instruments, the filter-analyzer is designed to investigate lattice dynamics and molecular vibrations over a

wide energy range and is particularly suited to measuring materials containing light elements such as hydrogen. In each of these instruments, the final energy is fixed using a low bandpass polycrystalline filter instead of the crystal analyzer that is traditionally used in the triple-axis instrument. The benefit of this sort of spectrometer is that smaller samples may be measured. The filter-analyzer technique provides an invaluable method for measuring the phonon density of states (DOS) (or vibrational density of states, vDOS), which serves as an important step in determining the fundamental properties of a material. Many thermophysical properties such as electrical properties,^{4,5} thermal conductivity,⁶ and diffusion depend on the vDOS. A preliminary understanding of more exotic magnetic⁷ and superconducting⁸ behavior may also be obtained through studies of the vDOS.

A number of enhancements and upgrades were made to the Taipan instrument in 2017: (i) addition of a second monochromator [Cu(200)] that increased the maximum incident energy from 70 to 200 meV, (ii) installation of a new tertiary shutter to improve the signal-to-noise ratio, and (iii) a sapphire-filter translation stage to

TABLE I. Computer software programs and packages used at major neutron sources for different stages of the data treatment process. Neutron instruments listed are all used to measure the vibrational density of states.

| Neutron instrument | Neutron source | Control software | Data treatment | Data analysis/visualization |
|-------------------------------------|----------------|------------------|----------------|-----------------------------|
| Tosca (spectrometer) | ISIS | IBEX | MANTID | |
| Vision (vibrational spectrometer) | ORNL | EPICS | MANTID | |
| LAGRANGE (triple-axis spectrometer) | ILL | NOMAD | NOMAD | Origin, MATLAB, excel, etc. |
| FANS (spectrometer) | NIST | ICP | DAVE | |
| Taipan (triple-axis spectrometer) | ANSTO | SICS | Gumtree | |

allow control of the incident neutron flux for energies greater than 80 meV.⁹

Construction of an instrument for use in a publicly funded, large-user facility is a lengthy process, requiring years of commissioning and testing to ensure that the instrument is sufficiently calibrated. In tandem with hardware developments, the software to operate the instrument must also be developed. Return on the investment of construction of these instruments is in the number of peer-reviewed journal publications produced as a result of reliable measurements. Due to the highly specialized nature of these instruments, it is often the case that only a few people are familiar with how to treat the data. This can form a bottleneck in the process of award of beam time → execution of experiment → data treatment → publication of results. One way to avoid this bottleneck is by implementing facility-wide data-treatment software for use on all instruments (diffractometers and spectrometers), which allows users and instrument scientists alike the opportunity to develop a familiarity with the software that comes pre-programmed for the instrument of choice. Such software can be implemented further, at multiple user facilities, thus allowing ease of exchange and comparison between datasets. This exchange becomes even more critical when measuring at continuous neutron sources, e.g., ILL, ANSTO, FRM-II, HZB, NIST, etc., than data obtained at pulsed neutron sources, e.g., ORNL, ISIS, ESS, etc.

The Institut Laue–Langevin implemented the instrument control software NOMAD,¹⁰ which includes a graphical user interface, providing end users with continuity when switching between different instruments. Other global neutron facilities such as ISIS (UK) and the Oak Ridge National Laboratory (USA) offer users the versatile neutron analysis software MANTID,¹¹ thus providing an even wider commonality for users regularly utilizing a number of international neutron sources. Another way to accelerate this process and subsequent publication of results is with the development of technique-specific strategies.^{12,13}

The operation software used to control most instruments at the Australian Centre for Neutron Scattering (ACNS)¹⁴ at the ANSTO is an adaptation of the Swiss Spallation Neutron Source (SINQ) Instrument Control Software (SICS) package¹⁵ while the user interface called “Gumtree” is secondary software often optimized to the individual instrument. Operation or control software is used to drive motors, activate air pads, etc., where user interface software will have data treatment and data analysis tools. A summary of both types of software currently in use at major neutron sources worldwide is provided in Table I.

Data collected at the Taipan filter-analyzer are processed by Gumtree whereby counts from the 30 position-sensitive detectors

can be integrated and subsequently normalized to beam monitor counts. While this is the output, as ASCII files, for more detailed data treatment, there is no “one-size fits all” strategy for the data treatment necessary for publication. As such, this paper seeks to set out the data-treatment steps required to generate reliable, instrument-calibrated, publishable data.

II. FILTER-ANALYZER NEUTRON SPECTROMETERS

There are five filter-analyzer neutron spectrometers currently in operation worldwide: Tosca, Vision, LAGRANGE, FANS, and Taipan; however, there are only three in operation at continuous source neutron facilities. While numerous time-of-flight instruments can also collect DOS and vDOS measurements, in this paper, we will introduce the five filter-analyzer spectrometers and focus on the latest filter-analyzer instrument to enter operation: the Taipan “Be-filter.”

A. Tosca, ISIS

Tosca is an indirect geometry spectrometer optimized for the study of molecular vibrations in the solid state. Tosca, the high-resolution crystal analyzer spectrometer, is installed and operated at the ISIS pulsed neutron source (Rutherford Appleton Laboratory, UK).¹⁶ ISIS maintains a database of vDOS spectra measured on Tosca and its predecessor, TXFA, from numerous well-known compounds and makes these publicly available.¹⁷

B. Vision, ORNL

Vision is the highest resolution broadband inelastic neutron scattering (INS) spectrometer in the world, installed and operated at the Oak Ridge National Laboratory pulsed neutron source in the USA. Vision is optimized to characterize molecular vibrations in a wide range of crystalline and disordered materials over a broad energy range (> 5 to <600 meV). This inverted geometry instrument offers enhanced performance by coupling a white beam of incident neutrons with two banks of seven analyzer modules, equipped with curved pyrolytic graphite crystal analyzer arrays that focus neutrons on a series of small detectors. This arrangement leads to an improved signal-to-noise ratio.¹⁸

C. Lagrange, ILL

IN1-LAGRANGE (Large Area GRAPHite Analyzer for Genuine Excitations) has been in operation since early 2010 at the Institut Laue–Langevin, the continuous source 60 MW reactor in France.

This clever design is a fresh take on filter spectrometers where a graphite filter is used in the reflection mode to scatter neutrons onto a central block of beryllium. Four different monochromators provide a wide energy transfer range, allowing measurement of the vDOS on a multitude of samples.^{19,20} Data reduction is managed by NOMAD such that users receive data that are ready for instant scientific analysis.

D. FANS, NIST

The Filter-Analyzer Neutron Spectrometer (FANS) is an instrument used for neutron vibrational spectroscopy installed at the continuous neutron source of the National Centre for Neutron Scattering (NCNR) in the USA. This instrument offers a choice of monochromators, a combination of polycrystalline Be followed by a bank of polycrystalline graphite analyzers cooled by liquid nitrogen to 77 K and an upstream Bi filter to reduce excitation of the Be filter banks from the scattered beam. This makes the FANS a versatile thermal-neutron scattering instrument at NIST.²¹

E. Taipan, “Be-filter” ANSTO

The ANSTO filter-analyzer was built based on FANS design but with sufficient differences between the two instruments to require a slightly different data-treatment process. Here, we will introduce the various factors that affect measurements taken with the Taipan filter-analyzer instrument. Overall, artifacts are generally created by the spectrometer optics, but the materials in the detector also have an effect on performance.

1. Detector materials

The Taipan monochromator is located 8 m away from the core of the OPAL 20 MW low-enriched uranium reactor. Extensive concrete and lead shielding is utilized to protect the instrument enclosure, providing a safe working environment for staff and users. During operation, at large scattering angles, the filter-analyzer detector comes within 1 m of these concrete walls; however, the shielding is sufficient that there is no increase in counts by detectors closer to the wall than when further away.

The filter spectrometer consists of four cooled filter banks arranged in an arc of $\sim 80^\circ$ centered around the sample, namely, bismuth, beryllium, graphite, and a second beryllium bank. These filter banks, including the radial collimator and the detectors, are all housed within a 1 m³ stainless steel vacuum chamber and maintained below 70 K. A diagram of this arrangement is given in Fig. 1. The pressure in the He³ detectors is deliberately lower than usual ($P = 2$ bar) so that efficiency is maintained for the very low energies but falls off significantly with increasing energy.

As well as the inelastic scattering occurring in the sample, a portion of the beam is also elastically scattered. A part of this goes through the Al window of the detector bank, which is 4 mm thick. Inelastic scattering from the aluminum density of states occurs here and gets detected as a sample-temperature-independent increase in intensity below 40 meV. This effect has been documented by NIST where it was determined that even the filter material right after the Al window can become a significant source of phonon contamination from these elastically scattered neutrons from the sample. Since Be was traditionally the first layer after the window, the spectra contained marked Be phonon contamination between 50 and 85 meV.

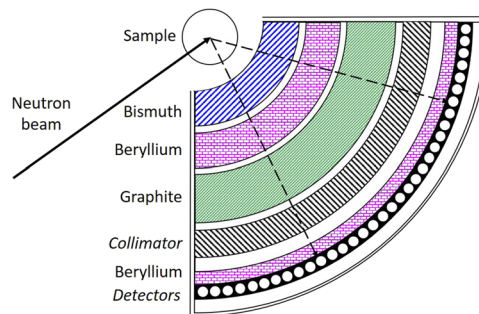


FIG. 1. Schematic diagram of the Taipan filter-analyzer detector bank at the ANSTO. The sample position and incoming direction of the neutron beam are included for clarity.

To mitigate this effect, an additional layer of polycrystalline Bi (with a Bragg cutoff similar to that of graphite) preceding the Be layer is found to be effective for filtering out the elastically scattered neutrons before they reach the Be.

2. Spectrometer optics

While the Taipan triple-axis instrument is well characterized, conversion to the filter-analyzer mode, and thus removal of the analyzer crystals, introduces a number of additional factors, which must be fully characterized. These arise from the variation in energy spread in the beam with the monochromator angle and second-order scattering, which results in wavelength contamination by the monochromators.

a. Energy variation correction. As the angle, θ , of the monochromator is changed, to provide the range of incident energies, there is a systematic variation in both energy, E , and wavelength, λ , spread in the beam. Starting with Bragg's law,

$$n\lambda = 2D \sin \theta, \quad (1)$$

where D has been used for the lattice spacing of the monochromator crystal, and using the known lattice spacings for individual monochromators from the relevant reflections, a table of angles and corresponding wavelengths can be generated. The lattice spacings for a selection of monochromators have been included in Table II for convenience. Values for θ can be input in 1° steps between the range $37^\circ < \theta < 10^\circ$ to generate an energy range (for the PG monochromator) of $5 < E_i < 60$ meV.

TABLE II. Lattice spacings of filter-analyzer monochromators and their associated energy transfer ranges.

| Neutron instrument | Monochromator | Lattice spacing, D (Å) | Energy transfer range, E (meV) |
|--------------------|---------------|--------------------------|----------------------------------|
| LAGRANGE | Cu (331) | 0.829 | 67–500 |
| | Si (111) | 3.135 | 4.5–20 |
| Taipan | PG (002) | 3.354 | 5–70 |
| | Cu (200) | 1.807 | 30–220 |
| FANS | Cu (220) | 1.278 | 5–250 |

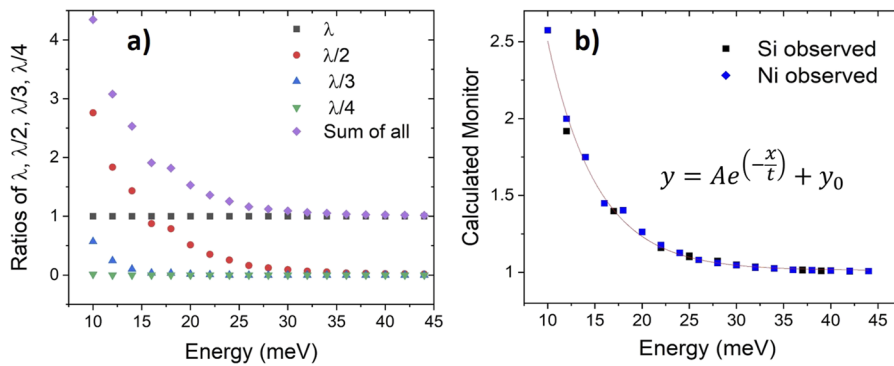


FIG. 2. Correction factor for the Taipan beam as a function of incident energy for the PG(002) monochromator indicating (a) the $\lambda/2$ and $\lambda/3$ components and (b) the correction factor for wavelength contamination (values for the constants are $A = 9.64047$, $t = 4.94769$, and $y_0 = 1.05681$).

To generate the error in the wavelength, it is necessary to take the differential of Bragg's law,

$$d\lambda = \lambda \cot \theta d\theta. \quad (2)$$

The value of $d\theta$ for Taipan was chosen to be 0.25° as this is approximately half the width of the collimation.

The error in the energy is obtained from the de Broglie relation of a neutron,

$$E_i = \frac{h^2}{2m_n\lambda^2}, \quad (3)$$

where h is Planck's constant and m_n is the mass of a neutron. This too must be differentiated, which results in the following equation:

$$dE_i = -2 \frac{d\lambda}{\lambda^3} \frac{h^2}{2m_n}, \quad (4)$$

where $d\lambda$ is the wavelength error obtained from Eq. (2). These four equations can be used to generate a table of values for the error in the incident energy over the full range of the monochromator rotation.

This step is necessary when one considers that many calculations of the vDOS are performed at equal energy intervals. The experimentally measured data must be converted so that they too have equal energy intervals. Our energy variation correction performs this conversion so that when data are compared, both experimental and calculated data have the same width as a function of energy.

b. Monochromator wavelength contamination. To understand the relative contributions of higher-order wavelengths due to multiple scattering from the monochromator, powder diffraction patterns could be collected. Since both the triple-axis and filter-analyzer spectrometers at Taipan utilize the same PG monochromator, this characterization was performed using both Si and Ni powder samples with the triple-axis spectrometer configuration. This allowed us to characterize the energy dependence of the PG monochromator. The data in Fig. 2 were collected by measuring counts across all scattering angles at 2 meV interval energies (E_i) in the range $10 < E_i < 42$ meV. Taipan was set in the two-axis mode, and the scattering angle was varied from 10° to 90° . Each of these datasets contained well characterized Bragg peaks from λ , $\lambda/2$, and $\lambda/3$. Rietveld refinement using these data was performed using GSAS,²² and the relative fractions of the different wavelengths were extracted by adjusting for both the

variation in the detector efficiency with wavelength and, for the case of nickel, the variation in its effective absorption with wavelength. These were normalized to the wavelength as illustrated in Fig. 2(a).

NB: The powder diffraction patterns were obtained using the Taipan triple-axis detectors ($P = 10$ bar) while the detectors shown in Fig. 1 are kept at a pressure of 2 bar.

The correction factor for higher order scattering should follow a decay law.²³ The data from Taipan were fit with a similar decay law to find the correction factor that needs to be applied to Taipan data [Fig. 2(b)]. By fitting the data, the effects of the sapphire filter on the reactor spectrum are included.

It is important to distinguish between higher-order scattering that occurs directly from the monochromator and that which occurs through interaction with the sample. The filter-analyzer detector is specifically designed to filter out higher-order scattering events from the sample. However, it may be unable to filter out any lambda scattering from the sample that has originated from a $\lambda/2$ scattering event from the monochromator. Thus, these higher order contributions must be considered, particularly at energies lower than 40 meV.²⁴

III. DATA TREATMENT

Considering the instrument factors from Sec. II E, there are three clear steps that users may consider implementing when treating the ANSTO "Be-filter" data. These steps seek performing an energy correction function (correcting for the physical location of the detector with respect to the neutron beam optics), removal of higher-order scattering due to higher-order wavelength contamination (monochromator crystal dependent), and background removal (dependent on the sample holder used). The effectiveness of these steps on existing datasets obtained on Taipan will be provided for a number of different sample types.

A. Pre-processing via Gumtree

At the ANSTO, on the Taipan filter-analyzer, Gumtree performs several critical data pre-processing steps. Gumtree displays multi-dimensional datasets (pulse-height profile and position profiles of each tube) in various formats, reducing data to 1D profiles that may be stored as ASCII files that are readable using various known post-processing software packages. Detector counts may also be normalized to monitor counts for comparison to other datasets.

The SICS control software allows for data acquisition in time as well as on a preselected number of monitor counts. Both modes have advantages depending on the application. Monitor counting does allow for an apparent constant number of neutrons to be counted at each energy level. Monitor sensitivity does, however, suffer from an inverse relationship with the velocity of the incident neutron, which should be considered. It is worth noting at this point that the filter-analyzer, by nature of its design (measuring $5 < E < 200$ meV), is sourced by a Maxwellian neutron flux distribution that peaks at ~ 40 meV.

B. Post-processing by the user

All post-processing must be conducted on datasets that have been first normalized to monitor. There then follows four key steps that the user should consider to undertake in order to treat their data. The four key steps are as follows:

1. background signal removal,
2. energy corrections,
3. wavelength contamination removal, and
4. energy transfer conversion.

1. Step 1: Background removal

For samples that do not contain any hydrogen, the signal is limited, and thus, it is important to maximize the amount of sample material in the beam while minimizing the amount of Al and other non-sample materials. Typically, the optimum neutron scattering sample is the one that scatters 10%–25% of the incoming neutron beam.²⁵ The corresponding thickness of the sample to achieve 10%–25% scattering follows Beer’s Law and is dependent on the total scattering cross section of all elements in the sample (a list of neutron cross sections is provided for some key elements in Table III). Equation (5) gives the relationship between the cross section and sample thickness for a 10% scatterer, i.e., $T = 0.1$,

$$T = \frac{I_f}{I_0} = \exp(-n_s \sigma t), \quad (5)$$

where T is the transmittance (i.e., the ratio of final (I_f) and incident (I_0) intensities of neutron radiation), n_s is the number density of atoms in the material, σ is the material cross section, and t is the thickness of the material.

TABLE III. Neutron scattering cross sections of selected elements.²⁶

| Element | Neutron cross sections (barn) | | |
|----------|-------------------------------|------------|--------|
| | Coherent | Incoherent | Total |
| Hydrogen | 1.7568 | 80.26 | 82.020 |
| Carbon | 5.551 | 0.001 | 5.551 |
| Nitrogen | 11.01 | 0.500 | 11.510 |
| Oxygen | 4.232 | 0.0008 | 4.232 |
| Aluminum | 1.495 | 0.008 | 1.503 |
| Silicon | 2.163 | 0.004 | 2.167 |
| Titanium | 7.485 | 0.550 | 8.030 |
| Copper | 1.485 | 2.870 | 4.350 |

Any material with a particularly large cross section will scatter well; those without will scatter less. With oxides, for example, it is likely that weak optical modes can be measured occurring at ~ 70 – 100 meV, but it is likely that the Al signal will contribute to the sample signal at lower energies. This is particularly noticeable when trying to measure a small amount of the sample and/or a low-scattering flux sample—the Al signal can dominate. It is important to minimize the Al signal that arises from both the sample can and the cryostat, since the collimation is very coarse.

If it has been unavoidable to use Al and/or if the data have already been obtained without an opportunity to remeasure, then the background signal arising from the empty sample container (which has been normalized-to-monitor counts), needs to be removed from the sample signal. This is carried out simply by subtracting the empty can scan from the sample scan. This is imperfect; unfortunately, as it does not take into account the change in the amount of material in the beam, however, to a good approximation, it should be sufficient to remove the Al signal.

2. Step 2: Energy corrections

All data obtained with any type of monochromator must be divided by the uncertainty in the energy ΔE obtained from the combined uncertainty in the incident and final energies to give the standard deviation as defined in the following equation:

$$dE = \sqrt{dE_i^2 + dE_f^2}, \quad (6)$$

where $dE_f = 0.5$ meV and dE_i values are calculated from Eq. (3). It is important to realize that the data provided by Gumtree are already in the form of E_i values. Hence, Eq. (4) must be rearranged, substituting λ for the Bragg relation, thus generating a list of monochromator angles. This is tedious, but necessary, particularly because the E_i values can be different for each and every scan as the motor driving the monochromator will not behave in exactly the same way with each movement.

If the conversion has been carried out correctly, values for the standard deviation should relate to the incident energy as per Fig. 3.

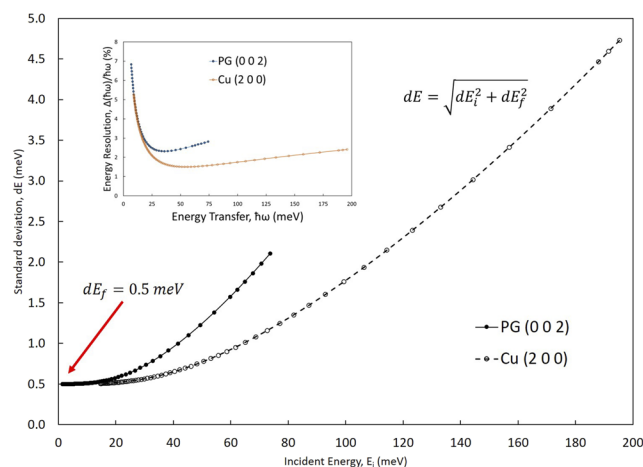


FIG. 3. Standard deviation of energy as a function of the incident energy for each monochromator. The inset shows the related energy resolution function for the Cu(200) and PG(002) monochromators on Taipan.

In addition, all data collected <50 meV must be *divided* by the exponential function given in the following equation:

$$y = Ae^{(-x/t)} + y_0, \quad (7)$$

where y is the output (scaled neutron counts), x is the incident energy value, and A , t , and y_0 are constants dependent on the monochromator used. Using Si and Ni samples, we obtained values of $A = 9.64047$, $t = 4.94769$, and $y_0 = 1.05681$ for the PG(002) monochromator. This step is the correction factor for higher order scattering. As the fraction of half-order and third-order contamination gets higher as the energy decreases, much of the contamination has effectively disappeared by ~ 35 – 40 meV (Fig. 1); therefore, these effects can be ignored above these energies. Each of the above data-processing steps is illustrated in Fig. 4(a).

3. Step 3: Wavelength contamination removal

As mentioned, both PG(002) and Cu(200) crystals suffer from both $\lambda/2$ and $\lambda/3$ wavelength contamination. This means that any higher energy features will appear at lower energies as spurious features or “weak ghost peaks” [Fig. 4(b)]. The exact positions of these ghost features associated with $\lambda/2$ contamination (which is $4\times$ the main incident energy) can be predicted simply by transposing the energy values of the measured spectra by transposing the spectra onto an energy scale that has been divided by 4. This effectively maps out a spectrum onto its original spectrum, assuming that the incident energy was $\lambda/2$ instead of λ . Of course, for $\lambda/3$ contamination ($9\times$ the main incident energy), it is necessary to divide by 9 instead of 4.

It is also necessary to reduce the intensity of the measured spectra when producing the transformed spectra. The intensity of the $\lambda/2$ data should be divided by 4, and the intensity of the $\lambda/3$ data should be divided by 9. The orange traces in 4(b) show how the Cu monochromator data are transposed in energy and intensity after such a transformation.

When performing the subtraction, it is possible that the resulting trace will produce negative values at lower energies. In this case, it may be necessary to reduce the intensity of the wavelength contamination even further.

Considering that we can only obtain information on the “ghost peaks” appearing in the PG spectrum by measuring with the Cu monochromator, this is an important experimental step. That is, in order to fully treat a PG spectrum with a maximum energy of 70 meV, data from the Cu monochromator would be ideally collected up to at least 70×4 meV = 280 meV. Practically, such a range is not possible with the Cu(200) reflection, a reason why the FANS utilizes a Cu(220) crystal as one of its monochromators (Table II). Nevertheless, users of the Taipan filter-analyzer should obtain data to the maximum Cu energy value to obtain the best results after data treatment at lower energies.

4. Step 4: Energy conversion

Finally, the x-axis must be converted from initial energy to energy transfer using the following simple equation:

$$\Delta E = \hbar\omega = E_i - E_f. \quad (8)$$

On Taipan, for the bismuth/beryllium/graphite filter combination, $E_f \leq 1.8$ meV. The final energy of the Taipan filter-analyzer detectors is taken to be 1.2 meV as this provides the best fit to data, and thus this value is taken for E_f . All that is required here is to subtract 1.2 meV from the every E_i value to obtain the energy transfer.

C. Case studies for different sample types

Here, we show the effectiveness of our post-processing treatment for different types of samples such as those with a high hydrogen content, those without any hydrogen and other relevant samples for condensed matter studies.

1. Case study: Hydrogen-rich compounds

Titanium dihydride is used as the absorber material in a hot carrier solar cell (HCSC), exploiting a large phonon bandgap sufficient to block the Klemens mechanism.²⁷ The Klemens decay mechanism is that where an optical phonon decays into two acoustic phonons with half the energy (and opposite momenta) of the original phonon. This decay route is restricted in materials where the energy gap between optical and acoustic phonons (phonon bandgap) is higher than the maximum acoustic phonon energy.²⁸ We measured a

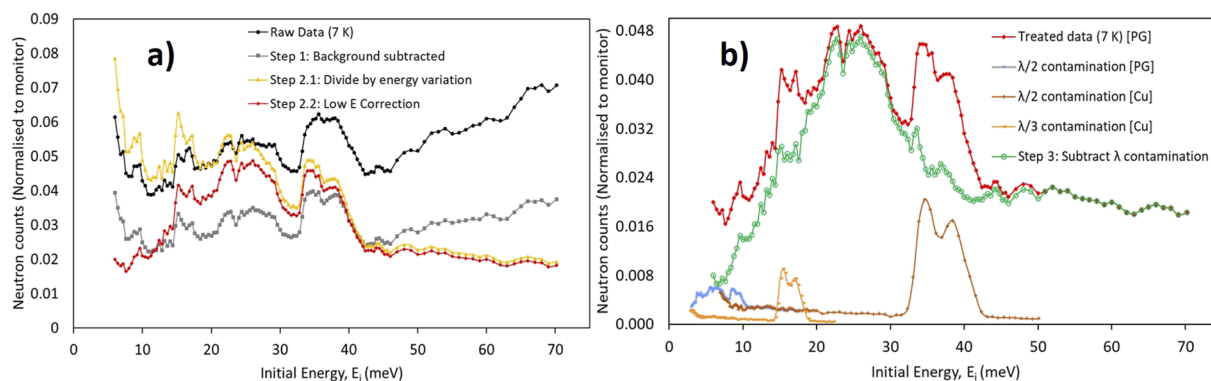


FIG. 4. Taipan filter-analyzer data of TiH_2 measured with the PG monochromator showing (a) post-processing output after background subtraction, energy variation, and low-energy corrections and (b) energy-corrected spectra (red) with wavelength contamination (blue) superimposed and removed (green) (red data are the same in both graphs but displayed on different scales).

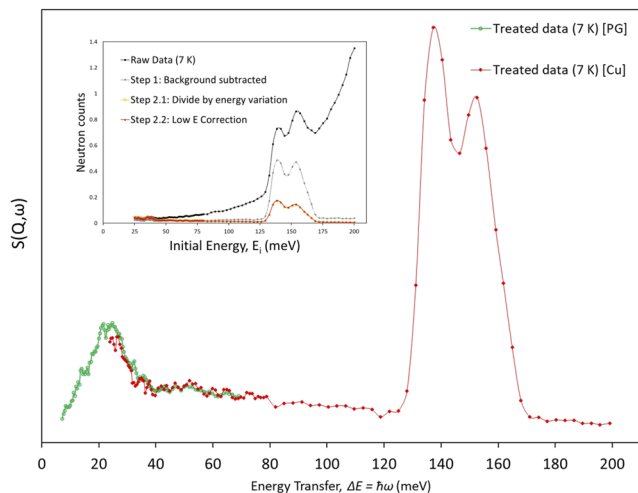


FIG. 5. Vibrational density of states data for TiH_2 measured with the Taipan filter-analyzer and fully treated to correct for various instrument effects. The inset shows the effect of each treatment step, i.e., background subtraction, energy corrections, and wavelength contamination removal.

sample of $\text{TiH}_{1.65}$ using the neutron time-of-flight spectrometer, “Pelican,” confirming a large (90 meV) bandgap between the upper edge of the acoustic phonon band and the lower edge of the optical phonon band.⁴ A more in-depth study of different stoichiometries of titanium hydrides is published elsewhere,²⁹ however, the sample TiH_2 serves as an excellent calibration sample for our purpose here.

In Fig. 5 the fully processed data of a TiH_2 sample are presented. The green trace shows data measured with the PG monochromator and is treated according to the four processing steps in Sec. III B. The inset details these steps as they relate to the Cu monochromator data. Here, the raw data measured with Taipan increase very steeply with increasing energy, an effect that is rectified with striking results when dividing by the energy variation correction. While it appears that the data are subject to exponential growth, the very intense vibrational mode may be fully recovered through the energy variation correction in Eq. (6). The data from the two monochromators show a good overlap, and the overall shape of the graph matches the theoretical predictions for the acoustic and optical bands in TiH_2 .³⁰ Importantly, the acoustic band contains two peaks at 25 meV and 38 meV, matching the two transverse phonon dispersion curves and one longitudinal phonon dispersion curve, respectively. The optical band between $130 < \Delta E < 170$ meV also has two peaks representing the two main branches of the optical phonon dispersion.

The wavelength contamination curves (orange) shown in Fig. 4(b) have been reduced in intensity from the original Cu monochromator data such that the intensity of the $\lambda/2$ data is four times smaller and the intensity of the $\lambda/3$ data is nine times smaller than the original spectrum. Contamination of the PG spectrum by its own $\lambda/2$ signal [blue, lower left Fig. 4(b)] is reasonably minor; however, it contributes to removing the peak at 10 meV—a feature that is not indicated by theoretical calculations. The green trace in Fig. 4(b) shows the effect of removing the three wavelength

contamination spectra from the red trace. It is clear to see that the two double “ghost peaks” are completely removed in this step.

In order to prevent negative values in the green trace, an additional factor of 2 had to be introduced to the intensity of the “ghost” spectra, i.e., $\lambda/2 \div (4 \times 2)$ and $\lambda/3 \div (9 \times 2)$.

Plotting the spectra from the two monochromators side by side in Fig. 5 shows a good overlap between the two datasets. The main acoustic peak at 27 meV now dominates the PG spectrum [a feature that was by no means obvious in the original raw data spectra (black) from 4(a)], and a second peak at 38 meV is also present. The overall spectrum now has the correct shape, i.e., a clear acoustic band in the energy range $0 < \Delta E < 40$ meV and a distinct optical band at $125 < \Delta E < 170$ meV. The phonon bandgap is clearly visible between the two bands, with a value of 85 meV, as predicted by theory.

2. Case study: Oxides

Minerals are compounds frequently studied with neutron scattering, both for their crystalline structure and water content. Opals are a fascinating area of research, and although a fundamental classification system³² has been used for almost 50 years, detailed knowledge of the structural relationships of the silica species involved remains elusive. With the structure $\text{SiO}_2 \cdot n\text{H}_2\text{O}$, the signal is dominated by scattering from hydrogen or, if desiccated, from the silica.

Using our data-processing steps, we have successfully treated a sample of Opal-CT, a paracrystalline form of opal often described as consisting of clusters of stacked cristobalite and tridymite over very short length scales, although the presence of cristobalite is contentious. The sample “G9887” is a honey opal from near Curdimurka, South Australia, Australia, which has been characterized with infrared methods³³ where no cristobalite was found in that sample. Figure 6(a) displays the plots of the opal raw data (black) and each subsequent spectra after each treatment step including background removal (gray), energy variation correction (yellow), low energy correction (red), lambda contamination (blue and orange), and removal (green). These data were obtained with the PG monochromator. The same steps were used to process the Cu monochromator data. All individual treatment steps of the Cu data are not shown here; only the fully processed spectra are presented in 6(b) (red trace).

The intensity of the $\lambda/2$ and $\lambda/3$ wavelength contamination peaks has been reduced by factors of 4 and 9, respectively; on this occasion, it was not necessary to include the factor 2 to prevent negative values. Figure 6(b) shows a good overlap of data between the PG (green) and Cu (red) monochromator data between 40 and 70 meV. The spectra of ice Ih (taken from the Tosca database³¹) are also provided (aqua) for comparison. The phonon dispersion for silica quartz has been simulated on many occasions,³⁴ indicating a phonon bandgap between 100 and 140 meV. While the opal data do show a decrease in the signal in this range, it does not drop to zero, so it is likely that this signal is due to the presence of water/ice. The position of some key peaks at 23, 28, and 38 meV also indicates a contribution from water. The calculated vDOS for SiO_2 also includes prominent peaks at 23 and 38 meV where the contribution to the acoustic band is actually dominated by oxygen while the strong peak at 70 meV has an equal contribution from Si and O.³⁵ The opal data presented

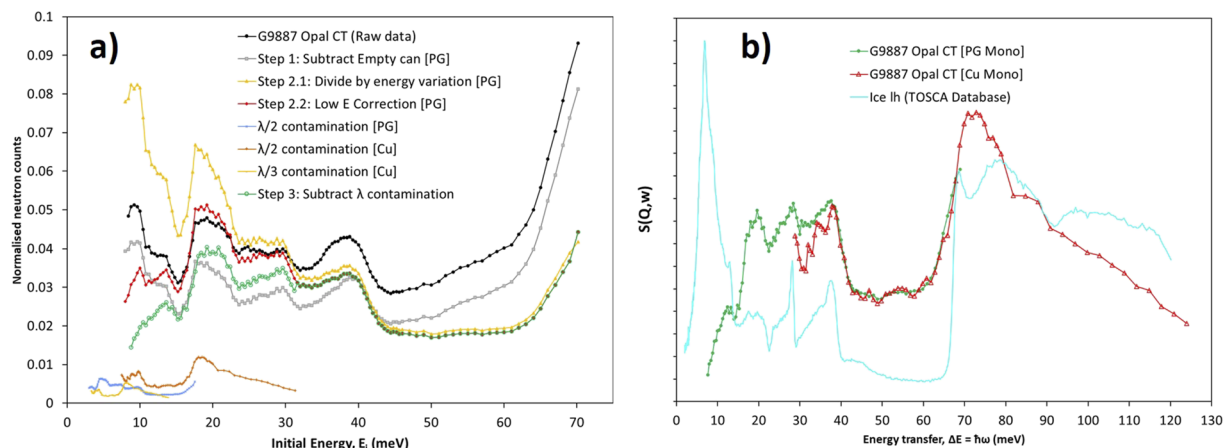


FIG. 6. Vibrational density of states data for the G9887 opal measured with the Taipan filter-analyzer neutron spectrometer and fully treated to correct for various instrument and background effects. (a) Data from the PG monochromator including wavelength contamination (orange and blue) and fully treated data (green). (b) Fully treated data from the PG (green) and Cu (red) monochromators including database spectra of ice Ih³¹ (aqua) taken from the Tosca database.

here are a selection from a full set obtained by another experimental group, who conducted a full analysis of the experimental data from a number of hydrated and desiccated opal samples and compared the theoretical vDOS of silica and experimental vDOS of water.³⁶

3. Case study: Metal-organic compounds

The international concern for reducing global CO₂ emissions has driven research into the development of solid porous

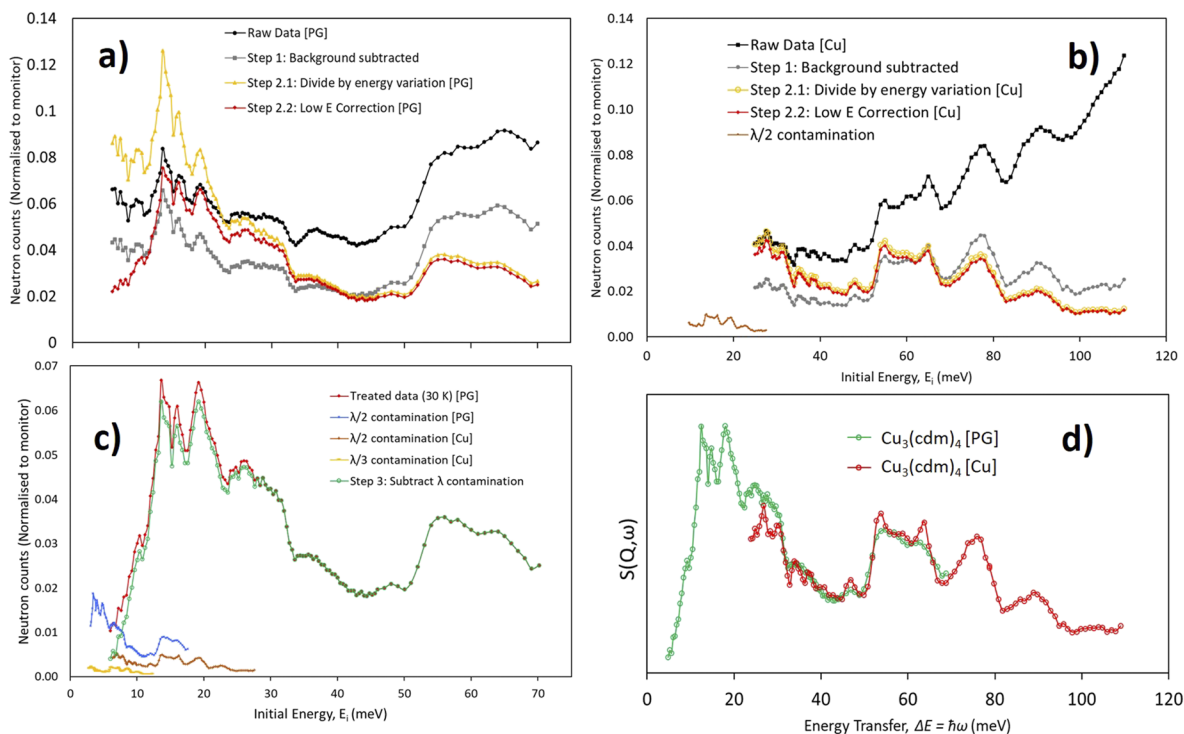


FIG. 7. Vibrational density of states data for $[\text{Cu}_3(\text{cdm})_4]$ ($\text{cdm} = \text{C}(\text{CN})_2(\text{CONH}_2)^-$) measured with the Taipan filter-analyzer neutron spectrometer and fully treated to correct for various instrument effects. Raw data and resulting spectra after each treatment step, i.e., background subtraction and energy corrections, are shown for the (a) PG and (b) Cu monochromators. Wavelength contamination and removal from the PG data are shown in (c) while (d) presents the full energy of data after conversion to energy transfer. NB: The red data spectra in (a) and (c) show the same data on different scales.

materials for the separation, storage, and potential conversion of CO_2 . Porous framework materials such as coordination polymers have attracted increasing attention for this application due to their capacity for structural modification, allowing their optimization for CO_2 selectivity and uptake. In order to advance these materials for this purpose, an understanding of the interactions between the host and their molecular guests is required, guiding the rational design of materials optimized for separation and storage performance. The ultramicroporous $\text{Cu}_3(\text{cdm})_4$ ($\text{cdm} = \text{C}(\text{CN})_2(\text{CONH}_2)^-$) material exhibits selectivity for CO_2 over other gases, including CH_4 , H_2 , and N_2 , and comprises approximately 4 Å diameter channels lined with coordinatively unsaturated Cu^{II} sites.³⁷ An understanding of guest interactions with $\text{Cu}_3(\text{cdm})_4$ was gained through neutron powder diffraction³⁸ and used as a basis for density functional theory (DFT)-based molecular dynamics (MD) simulations that provided further insight into the $\text{Cu}_3(\text{cdm})_4$ material function.³⁹ Ideally, the calculated atomic trajectories should be validated with the experimentally measured neutron vibrational spectrum, which also allows greater detail for low energy modes (such as those underpinning the property of negative thermal expansion), which is relatively commonly observed to be gained by these systems.⁴⁰ To this end, spectra for a $\text{Cu}_3(\text{cdm})_4$ sample were measured at 30 K on the Be filter instrument and treated using the steps outlined in Sec. II. The sample was first treated by heating under vacuum to remove all guest species and then was isolated from the atmosphere before and during measurement.

Figures 7(a)–7(d) show the experimentally collected data and their treatment. Figures 7(a)–7(c) show the raw data and the result of background removal and energy correction. Figure 7(c) plots wavelength contamination (lower left) and the result of subtracting this contamination from the PG monochromator data. In graphs (a) and (c), the red trace is the same data on a different scale. The wavelength contamination in the Cu monochromator data does not affect the data significantly. The highest measured energy is 110 meV, yielding 27.5 meV when divided by 4, indicating that only the first few datapoints are affected by $\lambda/2$ contamination subtraction. The intensity of the wavelength contamination had to be further reduced by a factor of 2, also to avoid negative values. As in the other case studies, data from both monochromators overlap in the range 40–50 meV. Figure 7(d) presents the corrected $S(Q, \omega)$ over the full energy range collected after these corrections.

DFT-based MD simulations of $\text{Cu}_3(\text{cdm})_4$ were performed using the Vienna *Ab initio* Simulation Package (VASP)⁴¹ with the projector augmented wave potential and the Perdew–Burke–Ernzerhof exchange–correlation functional, with the DFT-D2 method and a plane wave energy cutoff of 300 eV. The simulated system consisted of a single unit cell, with lattice parameters fixed to those determined by neutron powder diffraction at 30 K. A $1 \times 1 \times 1$ Monkhorst–Pack k-point mesh was defined, and the input structure was first optimized using the RMM-DIIS algorithm with a convergence threshold of 5×10^{-4} eV.

Preliminary simulations were conducted in the NVT ensemble for at least 5 ps (with 1 fs steps) before continuing in the NVE ensemble at 30 K for 30 ps. The first 5 ps of the NVE simulation were discarded, and simulated neutron $S(Q, \omega)$ was produced from the resulting trajectories using the program NMoldyn, with peak widths of 1, 3, and 5 meV. All details can be found elsewhere.³⁹ Simulated

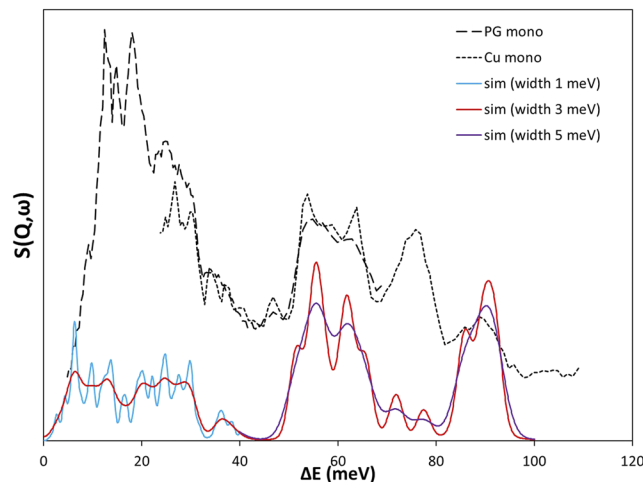


FIG. 8. Simulated and corrected experimental $S(Q, \omega)$. DFT-based MD simulations of $\text{Cu}_3(\text{cdm})_4$ calculated using the VASP.

and corrected experimental scattering $S(Q, \omega)$ are shown in Fig. 8, where many features of the simulated spectra are reconcilable with the experimentally measured data only after correction, demonstrating the effectiveness of steps taken in the correction of the Be-filter data.

IV. CONCLUSION

Clear data-treatment processes are necessary for the timely and trusted publication of scientific data from large-user facilities. An in-depth understanding of the operational features of a neutron instrument is required in order to create such a process, while merely knowing the treatment steps is sufficient for the user community. Until now, the Taipan Be-filter spectrometer has been used to perform high-quality scientific measurements, which have not been published due to the complexity of the data-treatment process. We have conducted multiple calibration measurements to characterize the instrument fully and identified all sources of spurious signals within the optics. This has led to the creation of a simple list of steps that users can take to treat their filter-analyzer data, which removes several instrument-based effects. Our data-treatment process involves four steps. The steps involved account for sample mounts, energy-corrections, second-order contamination arising from the monochromators, and conversion to neutron energy transfer. In certain circumstances, the intensity of the wavelength contamination must be further reduced by a factor of 2. We have demonstrated the effectiveness of these steps with three case studies of a hydrogen-rich sample (polycrystalline TiH_2 powder), an oxide-rich mineral (opal single-crystal), and a metal–organic framework material. It is critical to consider which monochromators have been used to generate the data as each one contributes to the signal in different ways. One way to avoid the contamination of the signal altogether would be to utilize a Ge (311) monochromator, which does not suffer from $\lambda/2$ contamination and provides an energy range of $10 < E_i < 300$ meV. Alternatively, Si with odd index planes would also be a smart choice, as utilized on LAGRANGE. In order for a

fully robust system of data analysis to be implemented, any experimental data must of course be compared with a well-constructed model. Any data output from a rigorous treatment process must still be compared with that generated by a scientific theory. It is our intention that the process we have developed here be helpful to all users of the Taipan filter-analyzer, thus ensuring that both regular and frequent user experiments on this rare and valuable neutron spectrometer can now be accompanied by a steady stream of peer-reviewed publications in the literature.

ACKNOWLEDGMENTS

We acknowledge financial support from the ANSTO via neutron proposals P5706, P6502 and P7361. We thank R.A. Mole, T.J. Udovic, and F. Franceschini for useful discussions.

DATA AVAILABILITY

Raw data were generated at the Australian Nuclear Science and Technology Organisation large scale facility. Derived data supporting the findings of this study are available from the corresponding author upon reasonable request.

REFERENCES

- 1 S. A. Danilkin, G. Horton, R. Moore, G. Braoudakis, and M. Hagen, "The TAIPAN thermal triple-axis spectrometer at the opal reactor," *J. Neutron Res.* **15**, 55–60 (2007).
- 2 A. P. J. Stampfl, A. Eltobaji, F. Darmann, and K. C. Rule, "The beryllium-filter spectrometer option on TAIPAN," *Neutron News* **27**, 27–29 (2016).
- 3 T. J. Udovic, D. A. Neumann, J. Leão, and C. M. Brown, "Origin and removal of spurious background peaks in vibrational spectra measured by filter-analyzer neutron spectrometers," *Nucl. Instrum. Methods Phys. Res. A* **517**, 189–201 (2004).
- 4 P. Wang, G. N. Iles, R. A. Mole, D. Yu, X. Wen, K.-F. Aguey-Zinsou, S. Shrestha, and G. Conibeer, "Hot carrier transfer processes in nonstoichiometric titanium hydride," *Jpn J. Appl. Phys.* **56**, 08MA10 (2017).
- 5 M. Mudge, B. K. Ng, C. J. Onie, M. Bhabbhade, R. A. Mole, K. C. Rule, A. P. J. Stampfl, and J. A. Stride, "What difference does a methyl group make: Pentamethylbenzene?," *ChemPhysChem* **15**, 3776–3781 (2014).
- 6 G. P. Cousland, R. A. Mole, M. M. Elcombe, X. Y. Cui, A. E. Smith, C. M. Stampfl, and A. P. J. Stampfl, "Investigation of the vibrational properties of cubic yttria-stabilized zirconia: A combined experimental and theoretical study," *J. Phys. Chem. Solids* **75**, 351–357 (2014).
- 7 I. G. Gurtubay, A. Iturbe-Beristain, and A. Eiguren, "Magnetic oscillations induced by phonons in non-magnetic materials," *Commun. Phys.* **3**, 22 (2020).
- 8 K.-P. Bohnen, R. Heid, and B. Renker, "Phonon dispersion and electron-phonon coupling in MgB₂ and AlB₂," *Phys. Rev. Lett.* **86**, 5771–5774 (2001).
- 9 K. C. Rule, F. Darmann, T. Oste, D. Bartlett, F. Franceschini, A. Berry, A. McGregor, A. Ogrin, T. Ersez, A. Kafes, S. Pangelis, S. Danilkin, A. P. J. Stampfl, and S. R. Olsen, "Recent enhancements and performance gains from upgrades to ANSTO's thermal neutron instrument TAIPAN and the triple-axis and Be-filter spectrometers," *Nucl. Instrum. Methods Phys. Res. A* **901**, 140–149 (2018).
- 10 P. Mutti, F. Cecillon, A. Elaazzouzi, Y. Le Goc, J. Locatelli, H. Ortiz, and J. Ratel, NOMAD – more than a simple sequencer, International Conference on Accelerator and Large Experimental Physics Control Systems (ICALEPCS-2011) No. INIS-FR-12-0750, ESRF (International Nuclear Information System, Grenoble, France, 2011).
- 11 O. Arnold, J. C. Bilheux, J. M. Borreguero, A. Buts, S. I. Campbell, L. Chapon, M. Doucet, N. Draper, R. Ferraz Leal, M. A. Gigg, V. E. Lynch, A. Markvardsen, D. J. Mikkelsen, R. L. Mikkelsen, R. Miller, K. Palmen, P. Parker, G. Passos, T. G. Per-ring, P. F. Peterson, S. Ren, M. A. Reuter, A. T. Savici, J. W. Taylor, R. J. Taylor, R. Tolchenov, W. Zhou, and J. Zikovsky, "Mantid—Data analysis and visualization package for neutron scattering and μ SR experiments," *Nucl. Instrum. Methods Phys. Res., Sect. A* **764**, 156–166 (2014).
- 12 F. Islam, J. Y. Y. Lin, R. Archibald, D. L. Abernathy, I. Al-Qasir, A. A. Campbell, M. B. Stone, and G. E. Granroth, "Super-resolution energy spectra from neutron direct-geometry spectrometers," *Rev. Sci. Instrum.* **90**, 105109 (2019).
- 13 J. Tao, C. J. Benmore, T. G. Worlton, J. M. Carpenter, D. Mikkelsen, R. Mikkelsen, J. Siewenie, J. Hammonds, and A. Chatterjee, "Time-of-flight neutron total scattering data analysis implemented in the software suite ISAW," *Nucl. Instrum. Methods Phys. Res., Sect. A* **562**, 422–432 (2006).
- 14 F. Klose, P. Constantine, S. J. Kennedy, and R. A. Robinson, "The neutron beam expansion program at the Bragg Institute," *J. Phys.: Conf. Ser.* **528**, 012026 (2014).
- 15 H. Heer, M. Koennecke, and D. Maden, "The SINQ instrument control software system," *Physica B* **241–243**, 124–126 (1997).
- 16 D. Colognesi, M. Celli, F. Cilloco, R. J. Newport, S. F. Parker, V. Rossi-Albertini, F. Sacchetti, J. Tomkinson, and M. Zoppi, "Tosca neutron spectrometer: The final configuration," *Appl. Phys. A* **74**, s64–s66 (2002).
- 17 Science and T. F. Council, INS database. A collection of INS spectra; accessed 24 June 06 2021.
- 18 P. A. Seeger, L. L. Daemen, and J. Z. Lares, "Resolution of vision, a crystal-analyzer spectrometer," *Nucl. Instrum. Methods Phys. Res., Sect. A* **604**, 719–728 (2009).
- 19 M. Jiménez-Ruiz, A. Ivanov, and S. Fuard, "LAGRANGE – The new neutron vibrational spectrometer at the ILL," *J. Phys.: Conf. Ser.* **549**, 012004 (2014).
- 20 A. Ivanov, M. Jimenez-Ruiz, and J. Kulda, "IN1-LAGRANGE – The new ILL instrument to explore vibration dynamics of complex materials," *J. Phys.: Conf. Ser.* **554**, 012001 (2014).
- 21 T. J. Udovic, C. M. Brown, J. B. Leão, P. C. Brand, R. D. Jiggerts, R. Zeitoun, T. A. Pierce, I. Peral, J. R. D. Copley, Q. Huang, D. A. Neumann, and R. J. Fields, "The design of a bismuth-based auxiliary filter for the removal of spurious background scattering associated with filter-analyzer neutron spectrometers," *Nucl. Instrum. Methods Phys. Res., Sect. A* **588**, 406–413 (2008).
- 22 A. C. Larson and R. B. von Dreele, "General Structure Analysis System (GSAS)," Los Alamos National Laboratory Report No. LAUR 86-748 (2000).
- 23 G. Shirane, S. M. Shapiro, and J. M. Tranquada, *Neutron Scattering with a Triple-Axis Spectrometer* (Cambridge University Press, 2006).
- 24 J. R. D. Copley, D. A. Neumann, and W. A. Kamitakahara, "Energy distributions of neutrons scattered from solid C₆₀ by the beryllium detector method," *Can. J. Phys.* **73**, 763–771 (1995).
- 25 S. F. Parker, D. Lennon, and P. W. Albers, *Vibrational Spectroscopy with Neutrons* (World Scientific Publishing Company, 2005).
- 26 V. F. Sears, "Neutron scattering lengths and cross sections," *Neutron News* **3**, 26–37 (1992).
- 27 P. G. Klemens, "Anharmonic decay of optical phonons," *Phys. Rev.* **148**, 845–848 (1966).
- 28 G. J. Conibeer, D. König, M. A. Green, and J. F. Guillemoles, "Slowing of carrier cooling in hot carrier solar cells," *Thin Solid Films* **516**, 6948–6953 (2008), part of the Special Issue: Proceedings on Advanced Materials and Concepts for Photovoltaics EMRS 2007 Conference, Strasbourg, France.
- 29 G. N. Iles, K. Chea, K. C. Rule, S. Russo, R. A. Mole, T. H. Nguyen, A. Stampfl, and M. M. Elcombe, "Dynamics in metallic hydrides measured with inelastic neutron scattering via the beryllium detector method" (2021) (unpublished).
- 30 V. I. Ivashchenko, L. A. Ivashchenko, P. L. Srynsckyy, L. A. Grishnova, and A. I. Stegnyy, "Ab initio study of the electronic structure and phonon dispersions for TiH₂ and ZrH₂," in *Carbon Nanomaterials in Clean Energy Hydrogen Systems*, edited by B. Baranowski, S. Y. Zaginichenko, D. V. Schur, V. V. Skorokhod, and A. Veziroglu (Springer Netherlands, Dordrecht, 2008), pp. 705–712.
- 31 J. Li, "Inelastic neutron scattering studies of hydrogen bonding in ices," *J. Chem. Phys.* **105**, 6733–6755 (1996).
- 32 J. B. Jones and E. R. Segnit, "The nature of opal I. Nomenclature and constituent phases," *J. Geol. Soc. Aust.* **18**, 57–68 (1971).
- 33 N. J. Curtis, J. R. Gascooke, and A. Pring, "Silicon-oxygen region infrared and Raman analysis of opals: The effect of sample preparation and measurement type," *Minerals* **11**, 173 (2021).
- 34 M. M. Elcombe, "Some aspects of the lattice dynamics of quartz," *Proc. Phys. Soc.* **91**, 947–958 (1967).

- ³⁵B. Wehinger, A. Bosak, K. Refson, A. Mirone, A. Chumakov, and M. Krisch, "Lattice dynamics of α -cristobalite and the Boson peak in silica glass," *J. Phys.: Condens. Matter* **27**, 305401 (2015).
- ³⁶N. Curtis, J. Gascooke, K. C. Rule, and A. Pring, "Inelastic neutron scattering study of opals" (2021) (unpublished).
- ³⁷L. J. McCormick, S. G. Duyker, A. W. Thornton, C. S. Hawes, M. R. Hill, V. K. Peterson, S. R. Batten, and D. R. Turner, "Ultramicroporous MOF with high concentration of vacant CuII sites," *Chem. Mater.* **26**, 4640–4646 (2014).
- ³⁸J. E. Auckett, S. G. Duyker, D. R. Turner, S. R. Batten, and V. K. Peterson, "Insights into selective gas sorbent functionality gained by using time-resolved neutron diffraction," *ChemPlusChem* **83**, 669–675 (2018).
- ³⁹J. E. Auckett, S. G. Duyker, E. I. Izgorodina, C. S. Hawes, D. R. Turner, S. R. Batten, and V. K. Peterson, "Anisotropic thermal and guest-induced responses of an ultramicroporous framework with rigid linkers," *Chem. – Eur. J.* **24**, 4774–4779 (2018).
- ⁴⁰S. G. Duyker, V. K. Peterson, G. J. Kearley, A. J. Ramirez-Cuesta, and C. J. Kepert, "Negative thermal expansion in LnCo(CN)₆ (Ln = La, Pr, Sm, Ho, Lu, Y): Mechanisms and compositional trends," *Angew. Chem., Int. Ed.* **52**, 5266–5270 (2013).
- ⁴¹G. Kresse and J. Furthmüller, "Efficient iterative schemes for ab initio total-energy calculations using a plane-wave basis set," *Phys. Rev. B* **54**, 11169–11186 (1996).